

Strain-tunable Dzyaloshinskii–Moriya interaction and skyrmions in two-dimensional Janus $\text{Cr}_2\text{X}_3\text{Y}_3$ ($\text{X}, \text{Y} = \text{Cl}, \text{Br}, \text{I}, \text{X} \neq \text{Y}$) trihalide monolayers

Zhong Shen, Changsheng Song,^{*} Yufei Xue, and Zebin Wu
Key Laboratory of Optical Field Manipulation of Zhejiang Province,
Department of Physics, Zhejiang Sci-Tech University, Hangzhou 310018, China

Jiqing Wang[†]
School of Physics and Electronic Science, East China Normal University, Shanghai 200241, China

Zhicheng Zhong[‡]
Key Laboratory of Magnetic Materials and Devices,
Zhejiang Province Key Laboratory of Magnetic Materials and Application Technology,
Ningbo Institute of Materials Technology and Engineering,
Chinese Academy of Sciences, Ningbo 315201, China and
China Center of Materials Science and Optoelectronics Engineering,
University of Chinese Academy of Sciences, Beijing 100049, China
(Dated: August 25, 2022)

Recently, great effort has been devoted to the search for two-dimensional (2D) ferromagnetic materials with inherent strong Dzyaloshinskii–Moriya interaction (DMI). Here, through a first-principles approach, we systematically investigate the effect of biaxial strain on the DMI, the Heisenberg exchange interaction, and the magnetic anisotropy energy (MAE) of Janus $\text{Cr}_2\text{X}_3\text{Y}_3$ ($\text{X}, \text{Y} = \text{Cl}, \text{Br}, \text{I}, \text{X} \neq \text{Y}$) monolayers. Both DMI and MAE can be significantly enhanced by tensile strain, while a reversal of the chirality of DMI in $\text{Cr}_2\text{Cl}_3\text{Br}_3$ and a switch of MAE from off-plane to in-plane in $\text{Cr}_2\text{I}_3\text{Cl}_3$ are induced by a compressive strain of 2%. Microscopically, DMI and MAE are associated mainly with the large spin–orbit coupling of the heavy nonmagnetic halogen atoms rather than that of the magnetic Cr atoms. In particular, the peculiar magnetic transition of $\text{Cr}_2\text{I}_3\text{Cl}_3$ is explained by competition between direct exchange and superexchange interactions. Micromagnetic simulations show that a small external magnetic field of 65 mT stabilizes a skyrmion with a diameter of 9.8 nm in the $\text{Cr}_2\text{I}_3\text{Cl}_3$ monolayer. Our results will provide guidance for further research on DMI and skyrmions in 2D Janus materials, as well as a basis for the potential applications in spintronic devices.

I. INTRODUCTION

Skyrmions are quasiparticles with unique topological protection characteristics and a vortex-like noncollinear spin texture with opposite directions between the central and edge spins [1–4]. Driven by a very small spin-polarized current, skyrmions can move accompanied by the skyrmion Hall effect [2, 5, 6]. These peculiar phenomena enable skyrmions to be used in a variety of new types of spintronic devices [7], such as track memory [8–10], microwave detectors [11, 12], and nano-oscillators [13, 14], among which track memory is expected to provide the next generation of nonvolatile, high-performance, low-energy-consumption, and high-density memory devices. The emergence and stability of magnetic skyrmions are mostly determined by the Dzyaloshinskii–Moriya interaction (DMI) [3], which is essentially a magnetic interaction caused by spin–orbit coupling (SOC) and breaking of spatial inversion symmetry.

Magnetic skyrmions were first found in single-crystal materials with $B20$ structure, such as MnGe [15] and

MnSi [16]. Later, it was discovered that magnetic skyrmions can exist in the more easily manipulated ultrathin metal layers with broken spatial inversion symmetry, such as $\text{Fe/Ir}(111)$ [17] and $\text{PdFe/Ir}(111)$ [18]. Since then, great effort has been made to calculate the magnetic parameters [19–21] and to grow ferromagnet/heavy metal (FM/HM) heterostructures, such as Pt/Co/MgO [22] and Ir/Fe/Co/Pt [23], whose interface DMI and off-plane magnetic anisotropy can be artificially adjusted by changing the film thickness, material combination, and other parameters [3].

However, for FM/HM heterostructures, their interfacial defects and atomic stacking order strongly affects the facial DMI [23] but are hard to control experimentally. Therefore, searching for and investigating 2D magnetic materials with intrinsic strong DMI is of great importance. Nonetheless, many 2D magnets are centrosymmetric with an absence of DMI, examples being CrI_3 [24, 25] and $\text{Cr}_2\text{Ge}_2\text{Te}_6$ [26]. Recently, a class of Janus materials with inherent broken spatial inversion symmetry have been reported to have strong SOC [27, 28] and large DMI that can stabilize skyrmions [29, 30].

Inspired by this, on the basis of the experimentally synthesized CrI_3 monolayer, we replace I atoms with Cl or Br to form Janus structures with intrinsic space inversion asymmetry. We demonstrate by first-principles cal-

^{*} cssong@zstu.edu.cn

[†] jqwang@ee.ecnu.edu.cn

[‡] zhong@nimte.ac.cn

culations that the DMI and magnetic anisotropy energy (MAE) of $\text{Cr}_2\text{X}_3\text{Y}_3$ ($X, Y = \text{Cl, Br, I}, X \neq Y$) monolayers can be greatly enhanced by the application of tensile strain. In particular, with a compressive strain of -2% , a chirality reversal of DMI and a switch of MAE from off-plane to in-plane appear in $\text{Cr}_2\text{Cl}_3\text{Br}_3$ and $\text{Cr}_2\text{I}_3\text{Cl}_3$, respectively. Microscopically, the strain-tunable DMI and MAE can be attributed to the strong SOC induced by the heavy nonmagnetic halogen atoms. Besides, the peculiar magnetic transition of $\text{Cr}_2\text{I}_3\text{Cl}_3$ is explained by the competition between direct exchange and superexchange interactions. In addition, micromagnetic simulations are performed with the magnetic parameters obtained from first-principles calculations, and a stable skyrmion with sub-10 nm diameter is found in an unstrained $\text{Cr}_2\text{I}_3\text{Cl}_3$ monolayer. Our work provides references for the study of skyrmions and DMI in 2D Janus monolayers, as well as guidance for spintronic applications.

II. CALCULATIONAL METHODS

A. First-principles calculations and micromagnetic simulation

We use the framework of density-functional theory (DFT) as implemented in the Vienna Ab initio Simulation Package (VASP) [31] to perform our first-principles calculations on $\text{Cr}_2\text{X}_3\text{Y}_3$ ($X, Y = \text{Cl, Br, I}, X \neq Y$) monolayers, with the projected augmented wave (PAW) method [32–34] describing the electron–core interaction. The generalized gradient approximation (GGA) of Perdew–Burke–Ernzerhof (PBE) [35] is chosen to treat the exchange correlation effects, with an effective Hubbard-like term $U = 3$ eV for $3d$ electrons of Cr [36–38]. The plane-wave cutoff energy is set as 500 eV, and the first Brillouin-zone integration is carried out using $9 \times 9 \times 1$ and $5 \times 10 \times 1$ Γ -centered k -point meshes for the primitive cell and the $2 \times 1 \times 1$ supercell, respectively. To obtain accurate DMI parameters, we set a high convergence standard, with the energy and force less than 10^{-6} eV and 0.001 eV/Å, respectively.

To explore the spin textures of the $\text{Cr}_2\text{X}_3\text{Y}_3$ system, we perform micromagnetic simulation with the Heisenberg model and Landau–Lifshitz–Gilbert (LLG) equation [39, 40] as implemented in the *Spirit* package [41]. A $70 \times 70 \times 1$ supercell with periodic boundary conditions is chosen, and the number of iterations is set to 2×10^5 to reach the stable state at each temperature point.

B. Dzyaloshinskii–Moriya interaction

To obtain the DMI strength, the chirality-dependent total energy difference approach [21, 28, 42, 43] is used, which has been successfully employed for DMI calculations in frustrated bulk systems and insulating chiral-lattice magnets, as well as in 2D Janus materials [43]. We

take a Hamiltonian with the following form [28, 43, 44]:

$$H = \sum_{\langle i,j \rangle} J_1(\vec{S}_i \cdot \vec{S}_j) + \sum_{\langle i,k \rangle} J_2(\vec{S}_i \cdot \vec{S}_k) + \sum_{\langle i,l \rangle} J_3(\vec{S}_i \cdot \vec{S}_l) + \sum_{\langle i,j \rangle} \vec{d}_{ij} \cdot (\vec{S}_i \times \vec{S}_j) + \sum_i K(S_i^z)^2. \quad (1)$$

Here, J_1 , J_2 , and J_3 are the Heisenberg exchange coefficients between nearest-neighbor, second-nearest-neighbor, and third-nearest-neighbor Cr atoms, and \vec{d}_{ij} is the DMI vector between spins \vec{S}_i and \vec{S}_j . K is the single-ion anisotropy coefficient, \vec{S}_i and \vec{S}_j are the spins of the i and j sites, and S_i^z is the z component of the spin at the i site.

As summarized by Moriya [45], if there is a mirror plane perpendicular to the Cr–Cr bond and passing through the middle of the bond, then the DMI vector \vec{d}_{ij} between the nearest-neighbor Cr atoms is in the mirror plane with the form

$$\vec{d}_{ij} = d_{\parallel}(\vec{u}_{ij} \times \vec{z}) + d_2\vec{z}, \quad (2)$$

where \vec{u}_{ij} and \vec{z} are the unit vectors from site i to site j and pointing along the z direction, respectively. Approximately, $\vec{d}_{ij} = \vec{d}_1 - \vec{d}_2$ [43, 46], where \vec{d}_1 , \vec{d}_2 will be explained in detail later [see Fig. 1(b)].

To evaluate the in-plane component d_{\parallel} , we choose the clockwise (CW) and anticlockwise (ACW) spin configurations with opposite chirality, as shown in Fig. 1(a) by yellow arrows. d_{\parallel} can be obtained from the following formula (a detailed derivation can be found in the Supplemental Material [47]):

$$d_{\parallel} = -\frac{E_{\text{CW}} - E_{\text{ACW}}}{4\sqrt{3}S^2}, \quad (3)$$

where E_{CW} and E_{ACW} are the energies of $\text{Cr}_2\text{X}_3\text{Y}_3$ monolayers with CW and ACW spin configurations, respectively, and S is the normalized spin [21]. To explore the microscopic physical mechanism of DMI, we calculate the SOC energy difference [21, 48] ΔE_{SOC} of $\text{Cr}_2\text{X}_3\text{Y}_3$ to see the contributions to DMI from different atoms. ΔE_{SOC} is extracted from the self-consistent total energy calculations of different spin configurations with opposite chirality when SOC is included.

III. RESULTS AND DISCUSSION

Top and side views of Janus $\text{Cr}_2\text{X}_3\text{Y}_3$ monolayers are shown in Fig. 1(a). The Cr atoms form a honeycomb network sandwiched by two nonmagnetic atomic planes with different halogen atoms X and Y . We now give a detailed description of the direction of the DMI. There are five rules to determine the direction of the DMI between two magnetic atoms A and B , with C being the midpoint of A and B , which are summarized by Moriya [45]. From Figs. 1(a) and 1(b), we can see that the symmetry

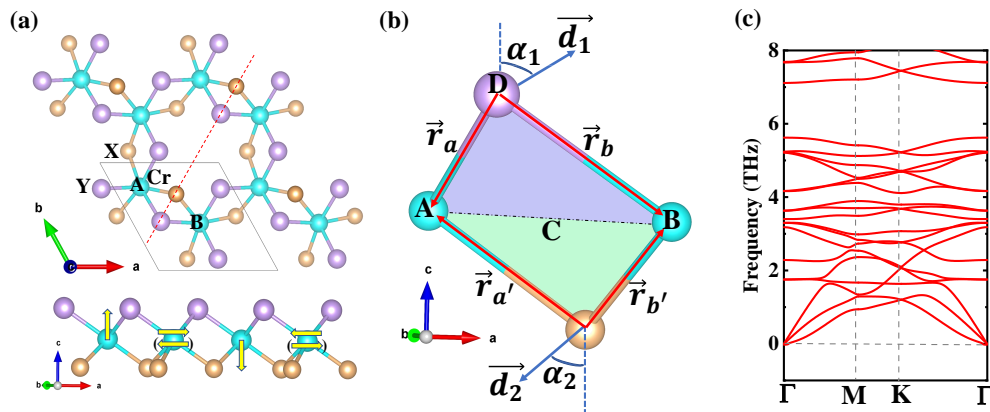


FIG. 1. (a) Top and side views of $\text{Cr}_2\text{X}_3\text{Y}_3$ ($X, Y = \text{Cl, Br, I}, X \neq Y$) monolayers. The solid lines in the top view show the primitive cell. A and B are the selected reference atoms, with the red dotted line being the mirror plane perpendicular to AB . The yellow vectors in the bottom view demonstrate the spin configurations to obtain the in-plane DMI component. (b) Schematic of \vec{d}_1 and \vec{d}_2 . D is a nonmagnetic halogen atom with strong SOC. $\vec{r}_a, \vec{r}_{a'}, \vec{r}_b,$ and $\vec{r}_{b'}$ are vectors from halogen atoms pointing to A or B , as shown by the red arrows. α_1 and α_2 are the angles between \vec{d}_1 and the z direction and between \vec{d}_2 and the z direction. (c) Phonon dispersion spectrum of $\text{Cr}_2\text{I}_3\text{Cl}_3$ along the high-symmetry points in reciprocal space.

of $\text{Cr}_2\text{X}_3\text{Y}_3$ satisfies the second of Moriya's symmetry rules: when a mirror plane perpendicular to AB passes through C , $\vec{d} \parallel$ mirror plane or $\vec{d} \perp AB$. However, this does not give us a precise direction of the DMI. Thus, from the further discussion in [46], we can determine the direction of \vec{d}_1 along $\vec{r}_b \times \vec{r}_a$ and \vec{d}_2 along $\vec{r}_{b'} \times \vec{r}_{a'}$, with $\vec{d} = \vec{d}_1 - \vec{d}_2$. Phonon dispersions are calculated to examine the stability of $\text{Cr}_2\text{X}_3\text{Y}_3$ in Fig. 1(c) and Fig. S1 (Supplemental Material [47]). There is no imaginary frequency in the case of $\text{Cr}_2\text{I}_3\text{Cl}_3$, which suggests that it is dynamically stable. The small imaginary frequencies of $\text{Cr}_2\text{Cl}_3\text{Br}_3$ and $\text{Cr}_2\text{I}_3\text{Br}_3$ indicate slight structural instability, which is often encountered in the phonon spectra of other 2D materials [43, 49].

As shown in Table I, the relaxed lattice constants a of $\text{Cr}_2\text{Cl}_3\text{Br}_3$, $\text{Cr}_2\text{I}_3\text{Cl}_3$, and $\text{Cr}_2\text{I}_3\text{Br}_3$ are 6.23, 6.55, and 6.73 Å, respectively, and they increase as functions of the radius of the nonmagnetic atoms X (Y). In our work, we do not further investigate the magnetic behaviors of $\text{Cr}_2\text{X}_3\text{Y}_3$ with compressive strain greater than 2%, because the DMI tends to become weaker as the compressive strain increases, which is not conducive to the creation of skyrmions.

We also notice that J_1 and J_2 of both $\text{Cr}_2\text{Cl}_3\text{Br}_3$ and $\text{Cr}_2\text{I}_3\text{Br}_3$ are negative in the range of -2% to 8% biaxial strain, as shown in Table I, while J_3 plays a less important role because it is more than an order of magnitude smaller than J_1 . According to Eq. (1), a negative value of the Heisenberg exchange coefficient corresponds to ferromagnetic (FM) coupling, while a positive value corresponds to antiferromagnetic (AFM) coupling. Thus, the ground states of $\text{Cr}_2\text{Cl}_3\text{Br}_3$ and $\text{Cr}_2\text{I}_3\text{Br}_3$ are FM in the range of biaxial strain from -2% to 8% . For the $\text{Cr}_2\text{I}_3\text{Cl}_3$ monolayer, we find that J_1 changes sign

twice when tensile strain is applied. To understand this peculiar behavior, we extract the energies of four spin configurations (*FM*, *Néel*, *Stripy*, and *Zigzag*) and calculate the bond angles of Cr–Cl–Cr (θ_1), Cr–I–Cr (θ_2) and the bond lengths of Cr–Cl (r_1), Cr–I (r_2), and Cr–Cr (r_3), as shown in Fig. 2. The system favors the FM configuration in the range of -2% to 3.5% biaxial strain. However, a transition from FM to AFM occurs at a strain of 4% , with the energy of the *Néel* AFM configuration being the lowest, as shown by the cyan area (II) in Fig. 2(b). Then, with increasing strain, another transition from AFM to FM appears at a strain of 6.5% , after which the system favors the FM configuration again. We notice that the trend of the change in energy of the *Néel* AFM configuration is similar to that of J_1 . We further explore the microscopic physical mechanisms of the transitions of J_1 using direct exchange and superexchange interaction theory [50–52]. As shown in Fig. 2(e), J_1 can be expressed as $J_1 = J_{S1} + J_{S2} + J_D$, where J_{S1} and J_{S2} represent the superexchange interactions of the paths Cr–I–Cr and Cr–Cl–Cr, and J_D represents the direct exchange interaction of Cr–Cr. Then, it can be seen from Fig. 2(c) that θ_1 and θ_2 are both close to 90° when the tensile strain is small. Thus, according to the Goodenough–Kanamori–Anderson (GKA) rules [50–52], both of the superexchange interactions J_{S1} and J_{S2} are FM ($J_{S1}, J_{S2} < 0$), whereas the direct exchange interaction J_D between nearest-neighbor Cr atoms is AFM ($J_D > 0$), and thus $J_1 = J_{S1} + J_{S2} + J_D$ has a negative value, corresponding to an FM coupling. Then, as the strain increases, θ_1 deviates from 90° , causing the FM superexchange interaction J_{S1} to become weak. A transition of J_{S1} from FM to AFM occurs when the strain increases further, as shown by the red dashed line in Fig. 2(f). This transition is caused mainly by the AFM

TABLE I. Optimized lattice constants a , angular difference $\Delta\theta$ between Cr–X–Cr (θ_1) and Cr–Y–Cr (θ_2), bond length difference Δr between Cr–X (r_1) and Cr–Y (r_2) [as shown in Fig. 2(e)], Heisenberg exchange coefficients J_1 , J_2 , J_3 , and magnetic moment M_{Cr} of Cr atoms in $\text{Cr}_2\text{X}_3\text{Y}_3$ monolayers with different strains.

	Strain (%)	a (Å)	$\Delta\theta$ (deg)	Δr (Å)	J_1 (meV)	J_2 (meV)	J_3 (meV)	M_{Cr} (μ_B)
$\text{Cr}_2\text{Cl}_3\text{Br}_3$	-2	6.11	9.21	0.17	-4.77	-0.62	0.16	3.01
	0	6.23	9.98	0.18	-4.37	-0.54	0.11	3.02
	2	6.36	10.62	0.19	-3.21	-0.47	0.07	3.04
	4	6.48	11.06	0.19	-1.91	-0.42	0.05	3.06
	6	6.61	11.42	0.19	-0.86	-0.38	0.03	3.08
	8	6.73	11.66	0.19	-0.26	-0.35	0.02	3.11
$\text{Cr}_2\text{I}_3\text{Br}_3$	-2	6.60	10.23	0.20	-5.50	-1.25	0.02	3.14
	0	6.73	10.77	0.21	-4.79	-1.11	-0.01	3.16
	2	6.87	11.04	0.21	-3.98	-1.00	-0.02	3.19
	4	7.00	11.16	0.21	-3.46	-0.91	-0.02	3.22
	6	7.14	11.19	0.20	-3.41	-0.84	-0.02	3.26
	8	7.27	10.10	0.18	-3.92	-0.78	-0.02	3.30
$\text{Cr}_2\text{I}_3\text{Cl}_3$	-2	6.42	20.57	0.39	-2.62	-1.26	-0.20	3.10
	0	6.55	21.47	0.39	-1.48	-1.09	-0.19	3.12
	2	6.68	22.01	0.39	-0.45	-0.96	-0.17	3.15
	4	6.81	22.22	0.39	0.17	-0.87	-0.14	3.18
	6	6.94	22.01	0.38	0.16	-0.80	-0.12	3.22
	8	7.08	21.31	0.36	-0.49	-0.75	-0.10	3.26

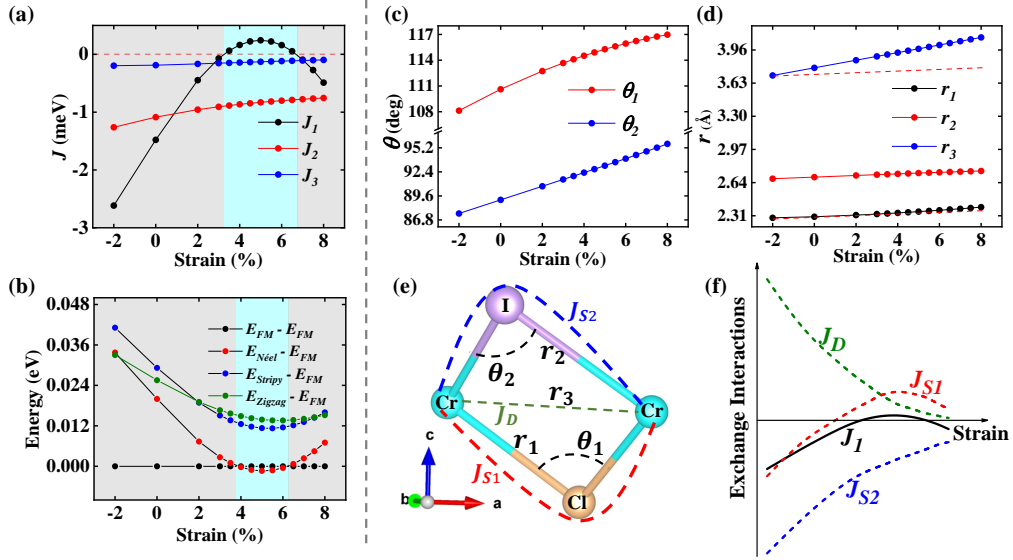


FIG. 2. (a) Heisenberg exchange coefficients J_1 , J_2 , J_3 , (b) energies of the four spin configurations (*FM*, *Néel*, *Stripy*, and *Zigzag*), (c) bond angles of Cr–Cl–Cr (θ_1) and Cr–I–Cr (θ_2), and (d) bond lengths of Cr–Cl (r_1), Cr–I (r_2), and Cr–Cr (r_3) as functions of biaxial strain. The red dashed line in (d) illustrates the slope of r_2 . (e) Schematic of θ_1 , θ_2 , r_1 , r_2 , r_3 , superexchange J_{S1} and J_{S2} , and direct exchange J_D . (f) Schematic of Heisenberg exchange interactions as functions of biaxial strain.

J_{S1} and J_D , which compete with the FM J_{S2} . Then, a second transition of J_1 from AFM to FM occurs, mainly as a result of the AFM J_{S1} and J_D decaying more rapidly than the FM J_{S2} . This can be attributed to the more rapid increases in r_1 and r_3 compared with r_2 , as shown in Fig. 2(d).

From the differences in bond angles ($\Delta\theta$) and bond lengths (Δr) in Table I, we can clearly see that the spatial inversion symmetry of Janus $\text{Cr}_2\text{X}_3\text{Y}_3$ is broken in

the off-plane direction. A large DMI can then be induced by the broken spatial inversion symmetry, as shown in Fig. 3(a). Here, we focus mainly on the in-plane component d_{\parallel} of the DMI, which plays a leading role compared with the off-plane component d_z (a comparison between d_{\parallel} and d_z can be found in Table S2 in the Supplemental Material [47]). As illustrated in Fig. 3(a), intrinsic large d_{\parallel} values of 0.38 and 0.36 meV are found in unstrained $\text{Cr}_2\text{I}_3\text{Cl}_3$ and $\text{Cr}_2\text{I}_3\text{Br}_3$ monolayers, respectively. Then,

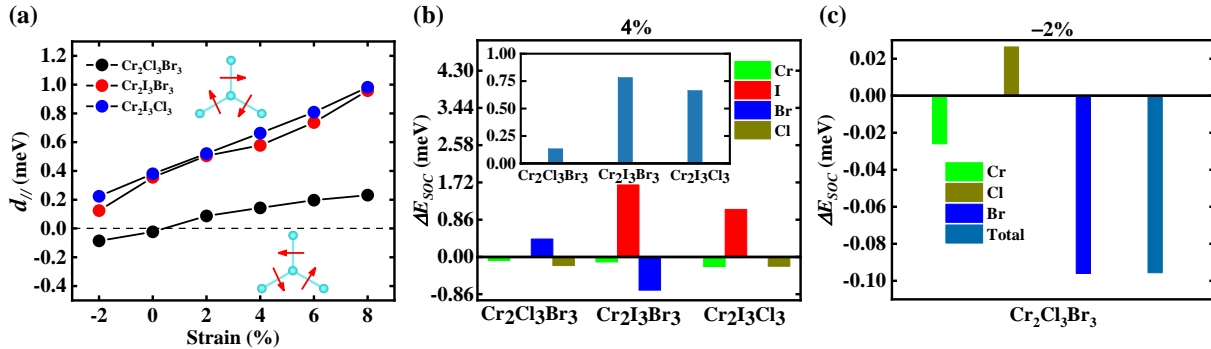


FIG. 3. (a) In-plane DMI component d_{\parallel} of $\text{Cr}_2\text{X}_3\text{Y}_3$ monolayers as a function of biaxial strain. The inset shows the d_{\parallel} (red arrow) between nearest-neighbor Cr atoms. (b) Atom-resolved localization of the SOC energy difference ΔE_{SOC} for $\text{Cr}_2\text{X}_3\text{Y}_3$ monolayers calculated with opposite chiralities under 4% biaxial strain and (c) that of $\text{Cr}_2\text{Cl}_3\text{Br}_3$ under -2% biaxial strain. The total SOC energy variation in each material is shown in the inset in (b).

with increasing biaxial strain, d_{\parallel} can be significantly enhanced up to 0.99 and 0.96 meV, which are more than two times larger than the values in the absence of strain. As shown by the inset in Fig. 3(a), positive and negative values of d_{\parallel} correspond respectively to CW and ACW arrangements of the in-plane DMI components.

To further understand the origin of strong DMI in $\text{Cr}_2\text{X}_3\text{Y}_3$ monolayers, as shown in Fig. 3(b), we calculate the DMI-associated SOC energy difference ΔE_{SOC} [21, 43] of different atoms in $\text{Cr}_2\text{X}_3\text{Y}_3$ at a tensile strain of 4%. The inset in Fig. 3(b) shows the algebraic sum of ΔE_{SOC} for each $\text{Cr}_2\text{X}_3\text{Y}_3$ monolayer, which corresponds to the strength of d_{\parallel} . Strong DMI is mainly associated with the large ΔE_{SOC} located on the heavy nonmagnetic halogen atom X or Y, which is similar to what occurs in Co/Pt [21] and MnXY [43] systems. Besides, in $\text{Cr}_2\text{X}_3\text{Y}_3$ monolayers, the ΔE_{SOC} of X and Y atoms have opposite signs, which can be explained by the Fert-Levy model [21, 43, 53]. Owing to the strong SOC of the halogen atoms X and Y, when a polarized electron transfers between Cr atoms through the intermediate atom X or Y, the spin direction of the electron is tilted by spin-orbit scattering, which leads to a tilt of local spins on adjacent Cr atoms. This tilt of local spins has two possibilities, namely, CW and ACW. When the local spins are tilted CW (ACW), $\Delta E_{\text{SOC}} = E_{\text{SOC}}^{\text{ACW}} - E_{\text{SOC}}^{\text{CW}} > 0$ ($\Delta E_{\text{SOC}} = E_{\text{SOC}}^{\text{ACW}} - E_{\text{SOC}}^{\text{CW}} < 0$). For halogen atoms on opposite sides of the Cr layer, the CW and ACW are also opposite, with the result that the ΔE_{SOC} of the X and Y atoms have opposite signs. Figure 3(c) shows the atom-resolved ΔE_{SOC} values of $\text{Cr}_2\text{Cl}_3\text{Br}_3$ for a strain of -2%. The results show that the ΔE_{SOC} of the Br atom plays a leading role, resulting in a negative total ΔE_{SOC} , which induces a negative d_{\parallel} in $\text{Cr}_2\text{Cl}_3\text{Br}_3$.

Not only do the DMI and Heisenberg exchange interaction affect the magnetic structure of 2D ferromagnets, but also the magnetic anisotropy plays a vital role in

the formation and stability of skyrmions. As we know, both the DMI and magnetic anisotropy originate from SOC. The magnetic anisotropy energy (MAE) is defined as the energy difference between in-plane (E_x) and off-plane (E_z) FM states: $\text{MAE} = E_x - E_z$, with $\text{MAE} > 0$ and $\text{MAE} < 0$ corresponding to off-plane and in-plane magnetic anisotropy (OMA and IMA), respectively. As shown in Fig. 4(a), the MAEs of $\text{Cr}_2\text{I}_3\text{Br}_3$ and $\text{Cr}_2\text{Cl}_3\text{Br}_3$ are positive and gradually increase as the strain changes from -2% to 8%. Interestingly, for the $\text{Cr}_2\text{I}_3\text{Cl}_3$ monolayer, there is a switch from OMA to IMA at a compression strain of -2%. To explore the microscopic physical mechanisms of MAE, we calculate the atom-resolved MAE of $\text{Cr}_2\text{I}_3\text{Cl}_3$ as a function of biaxial strain. As shown in Fig. 4(b), the heavy nonmagnetic atom I rather than the magnetic atom Cr makes the most significant contribution to MAE. A similar phenomenon has been found in CrI_3 [54, 55] and CrXTe (X = S, Se) [28] systems. Furthermore, we calculate the orbit-resolved MAE of the p orbitals of the I atom in $\text{Cr}_2\text{I}_3\text{Cl}_3$ at strains of 0% [Fig. 4(c)] and 4% [Fig. 4(d)]. At a strain of 0%, the hybridization between p_x and p_y orbitals contributes to positive MAE (OMA), while the hybridized p_x and p_z orbitals contribute to negative MAE (IMA). The competition between the hybridized p_x - p_y and p_x - p_z leads to the small OMA ($\text{MAE} > 0$) of $\text{Cr}_2\text{I}_3\text{Cl}_3$ at a strain of 0%. In the case of a strain of 4%, both the hybridization of p_x - p_y and that of p_x - p_z contribute to OMA, and the OMA contribution from p_x and p_y hybridization is enhanced more than twofold, which is responsible for the large OMA at a strain of 4%.

With the magnetic parameters obtained from a first-principles approach, we perform micromagnetic simulations with the Landau-Lifshitz-Gilbert (LLG) equation [39, 40] in the framework of *Spirit* [41]. As shown in Fig. 5(a), when no magnetic field is applied, we obtain wide domains separated by Néel-type domain walls.

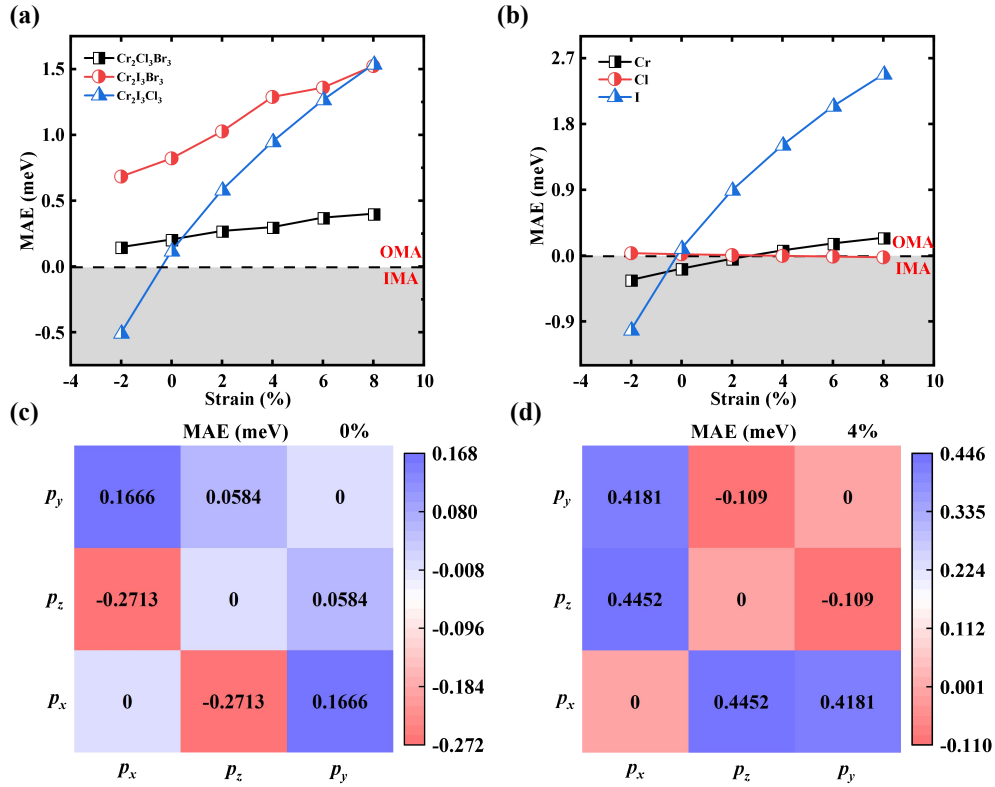


FIG. 4. (a) Total MAE of Janus $\text{Cr}_2\text{X}_3\text{Y}_3$ monolayers and (b) atom-resolved MAE of $\text{Cr}_2\text{I}_3\text{Cl}_3$ as functions of biaxial strain. (c) and (d) Orbit-resolved MAE of the $5p$ orbitals of the I atom in $\text{Cr}_2\text{I}_3\text{Cl}_3$ with 0% and 4% biaxial strain, respectively.

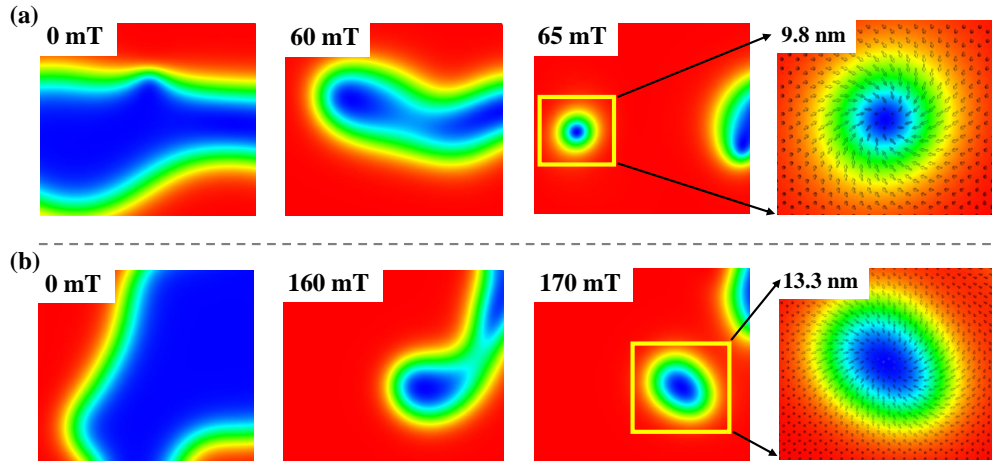


FIG. 5. Spin textures of $\text{Cr}_2\text{I}_3\text{Cl}_3$ at strains of (a) 0% and (b) 2% under different applied magnetic fields.

Then, with a small magnetic field of 60 mT, the spin-down domain shrinks to a wormlike one. When the magnetic field is increased further to 65 mT, an isolated skyrmion is induced, with a small diameter of 9.8 nm. Figure 5(b) shows the evolution of spin textures in $\text{Cr}_2\text{I}_3\text{Cl}_3$ under different applied magnetic fields at a

strain of 2%. Similar to the case at a strain of 0%, a small-sized skyrmion with a diameter of 13.3 nm can be induced by a magnetic field of 170 mT. Such a small skyrmion (~ 10 nm) is technologically desirable, since it can significantly enhance the storage density of skyrmion-based next-generation information memory devices [56, 57].

IV. CONCLUSIONS

To sum up, by first-principles calculations and micro-magnetic simulations, we have investigated in detail the magnetic parameters and spin textures of Janus $\text{Cr}_2\text{X}_3\text{Y}_3$ monolayers under biaxial strain. We have found that the DMI and MAE can be significantly enhanced by tensile strain. With a compressive strain of -2% , a chirality reversal of DMI and a switch of MAE from off-plane to in-plane appear in $\text{Cr}_2\text{Cl}_3\text{Br}_3$ and $\text{Cr}_2\text{I}_3\text{Cl}_3$, respectively. We have also explored the microscopic physical mechanisms of DMI and MAE in view of the strong SOC induced by the heavy nonmagnetic halogen atoms. In particular, we have explained the mechanisms of the peculiar magnetic transition in the $\text{Cr}_2\text{I}_3\text{Cl}_3$ monolayer in

terms of direct exchange and superexchange interactions. Moreover, in the unstrained $\text{Cr}_2\text{I}_3\text{Cl}_3$ monolayer, an isolated skyrmion with sub-10 nm diameter has been found which is desirable for spintronic applications. Our work has enlarged the family of 2D Janus materials, as well as providing guidance for further research on the DMI and chiral spin textures.

ACKNOWLEDGMENTS

This work was supported by the National Natural Science Foundation of China (No. 11804301), the Natural Science Foundation of Zhejiang Province (No. LY21A040008), and the Fundamental Research Funds of Zhejiang Sci-Tech University (No. 2021Q043-Y).

-
- [1] B. Göbel, I. Mertig, and O. A. Tretiakov, *Phys. Rep.* **895**, 1 (2021).
- [2] Y. Liu, Z. H. Qian, and J. G. Zhu, *Acta Phys. Sin.* **69**, 231201 (2020).
- [3] Y.-Z. Liu and J. Zang, *Acta Phys. Sin.* **67**, 131201 (2018).
- [4] M. Hoffmann, B. Zimmermann, G. P. Muller, D. Schurhoff, N. S. Kiselev, C. Melcher, and S. Blügel, *Nat. Commun.* **8**, 308 (2017).
- [5] P. Ao and D. J. Thouless, *Phys. Rev. Lett.* **70**, 2158 (1993).
- [6] W. J. Jiang, X. C. Zhang, G. Q. Yu, W. Zhang, X. Wang, M. B. Jungfleisch, J. E. Pearson, X. M. Cheng, O. Heinonen, K. L. Wang, Y. Zhou, A. Hoffmann, and S. G. E. te Velthuis, *Nat. Phys.* **13**, 162 (2017).
- [7] X. Zhang, Y. Zhou, K. Mee Song, T. E. Park, J. Xia, M. Ezawa, X. Liu, W. Zhao, G. Zhao, and S. Woo, *J. Phys.: Condens. Matter* **32**, 143001 (2020).
- [8] M. Mochizuki and S. Seki, *Phys. Rev. B* **87**, 134403 (2013).
- [9] Z.-P. Hou, B. Ding, H. Li, G.-Z. Xu, W.-H. Wang, and G.-H. Wu, *Acta Phys. Sin.* **67**, 137509 (2018).
- [10] S. S. Parkin, M. Hayashi, and L. Thomas, *Science* **320**, 190 (2008).
- [11] Y. Okamura, F. Kagawa, M. Mochizuki, M. Kubota, S. Seki, S. Ishiwata, M. Kawasaki, Y. Onose, and Y. Tokura, *Nat. Commun.* **4**, 2391 (2013).
- [12] G. Finocchio, M. Ricci, R. Tomasello, A. Giordano, M. Lanuzza, V. Puliafito, P. Burrascano, B. Azzerboni, and M. Carpentieri, *Appl. Phys. Lett.* **107**, 262401 (2015).
- [13] Z. Zeng, G. Finocchio, and H. Jiang, *Nanoscale* **5**, 2219 (2012).
- [14] R. H. Liu, W. L. Lim, and S. Urazhdin, *Phys. Rev. Lett.* **114**, 137201 (2015).
- [15] S. Muhlbauer, B. Binz, F. Jonietz, C. Pfleiderer, A. Rosch, A. Neubauer, R. Georgii, and P. Boni, *Science* **323**, 915 (2009).
- [16] F. Jonietz, S. Muhlbauer, C. Pfleiderer, A. Neubauer, W. Munzer, A. Bauer, T. Adams, R. Georgii, P. Boni, R. A. Duine, K. Everschor, M. Garst, and A. Rosch, *Science* **330**, 1648 (2010).
- [17] S. Heinze, K. von Bergmann, M. Menzel, J. Brede, A. Kubetzka, R. Wiesendanger, G. Bihlmayer, and S. Blügel, *Nat. Phys.* **7**, 713 (2011).
- [18] E. Simon, K. Palotas, L. Rozsa, L. Udvardi, and L. Szunyogh, *Phys. Rev. B* **90**, 094410 (2014).
- [19] L. Udvardi, L. Szunyogh, K. Palotas, and P. Weinberger, *Phys. Rev. B* **68**, 104436 (2003).
- [20] H. J. Xiang, E. J. Kan, S.-H. Wei, M. H. Whangbo, and X. G. Gong, *Phys. Rev. B* **84**, 224429 (2011).
- [21] H. Yang, A. Thiaville, S. Rohart, A. Fert, and M. Chshiev, *Phys. Rev. Lett.* **115**, 267210 (2015).
- [22] O. Boule, J. Vogel, H. Yang, S. Pizzini, D. de Souza Chaves, A. Locatelli, T. O. Mendes, A. Sala, L. D. Buda-Prejbeanu, O. Klein, M. Belmeguenai, Y. Roussigne, A. Stashkevich, S. M. Cherif, L. Aballe, M. Foerster, M. Chshiev, S. Auffret, I. M. Miron, and G. Gaudin, *Nat. Nanotechnol.* **11**, 449 (2016).
- [23] A. Soumyanarayanan, M. Raju, A. L. Gonzalez Oyarce, A. K. C. Tan, M. Y. Im, A. P. Petrovic, P. Ho, K. H. Khoo, M. Tran, C. K. Gan, F. Ernult, and C. Panagopoulos, *Nat. Mater.* **16**, 898 (2017).
- [24] B. Huang, G. Clark, E. Navarro-Moratalla, D. R. Klein, R. Cheng, K. L. Seyler, D. Zhong, E. Schmidgall, M. A. McGuire, D. H. Cobden, W. Yao, D. Xiao, P. Jarillo-Herrero, and X. Xu, *Nature* **546**, 270 (2017).
- [25] P. Jiang, L. Li, Z. Liao, Y. X. Zhao, and Z. Zhong, *Nano Lett.* **18**, 3844 (2018).
- [26] C. Song, W. Xiao, L. Li, Y. Lu, P. Jiang, C. Li, A. Chen, and Z. Zhong, *Phys. Rev. B* **99**, 214435 (2019).
- [27] J. Liang, W. Wang, H. Du, A. Hallal, K. Garcia, M. Chshiev, A. Fert, and H. Yang, *Phys. Rev. B* **101**, 184401 (2020).
- [28] Q. Cui, J. Liang, Z. Shao, P. Cui, and H. Yang, *Phys. Rev. B* **102**, 094425 (2020).
- [29] J. Yuan, Y. Yang, Y. Cai, Y. Wu, Y. Chen, X. Yan, and L. Shen, *Phys. Rev. B* **101**, 094420 (2020).
- [30] Y. Zhang, C. Xu, P. Chen, Y. Nahas, S. Prokhorenko, and L. Bellaiche, *Phys. Rev. B* **102**, 241107(R) (2020).
- [31] G. Kresse and J. Furthmüller, *Phys. Rev. B* **54**, 11169 (1996).

- [32] G. Kresse and J. Furthmüller, *Comput. Mater. Sci.* **6**, 15 (1996).
- [33] G. Kresse and J. Hafner, *Phys. Rev. B* **49**, 14251 (1994).
- [34] G. Kresse and J. Hafner, *Phys. Rev. B* **47**, 558 (1993).
- [35] J. P. Perdew, K. Burke, and M. Ernzerhof, *Phys. Rev. Lett.* **77**, 3865 (1996).
- [36] A. K. Behera, S. Chowdhury, and S. R. Das, *Appl. Phys. Lett.* **114**, 232402 (2019).
- [37] A. I. Liechtenstein, V. I. Anisimov, and J. Zaanen, *Phys. Rev. B* **52**, R5467 (1995).
- [38] J. Shang, X. Tang, X. Tan, A. Du, T. Liao, S. C. Smith, Y. Gu, C. Li, and L. Kou, *ACS Appl. Nano Mater.* **3**, 1282 (2019).
- [39] L. D. L. Lifshitz and E. M., *Physik Z. Sowjetunion* **8**, 51 (1935).
- [40] T. L. Gilbert, *IEEE Trans. Magn.* **40**, 3443 (2004).
- [41] G. P. Müller, M. Hoffmann, C. Dißelkamp, D. Schürhoff, S. Mavros, M. Sallermann, N. S. Kiselev, H. Jónsson, and S. Blügel, *Phys. Rev. B* **99**, 224414 (2019).
- [42] H. Yang, G. Chen, A. A. C. Cotta, A. T. N'Diaye, S. A. Nikolaev, E. A. Soares, W. A. A. Macedo, K. Liu, A. K. Schmid, A. Fert, and M. Chshiev, *Nat. Mater.* **17**, 605 (2018).
- [43] J. Liang, W. Wang, H. Du, A. Hallal, K. Garcia, M. Chshiev, A. Fert, and H. Yang, *Phys. Rev. B* **101**, 184401 (2020).
- [44] S. I. Vishkayi, Z. Torbatian, A. Qaiumzadeh, and R. Asgari, *Phys. Rev. Mater.* **4**, 094004 (2020).
- [45] T. Moriya, *Phys. Rev.* **120**, 91 (1960).
- [46] F. Keffer, *Phys. Rev.* **126**, 896 (1962).
- [47] See Supplemental Material at [URL will be inserted by publisher] for (1) phonon dispersion spectra of $\text{Cr}_2\text{Cl}_3\text{Br}_3$ and $\text{Cr}_2\text{I}_3\text{Br}_3$; (2) calculational details of the DMI, micro-magnetic DMI coefficient D and Heisenberg coupling coefficients; (3) relationship between DMI, MAE and SOC strength; (4) detailed lattice parameters and specific values of DMI.
- [48] A. Hallal, H. X. Yang, B. Dieny, and M. Chshiev, *Phys. Rev. B* **88**, 184423 (2013).
- [49] Y. C. Cheng, Z. Y. Zhu, M. Tahir, and U. Schwingenschlögl, *Europhys. Lett.* **102**, 57001 (2013).
- [50] B. Goodenough, *Phys. Rev.* **100**, 564 (1955).
- [51] J. Kanamori, *J. Phys. Chem. Solids* **10**, 87 (1959).
- [52] P. Anderson, *Phys. Rev.* **115**, 2 (1959).
- [53] A. Fert and P. M. Levy, *Phys. Rev. Lett.* **44**, 1538 (1980).
- [54] J. L. Lado and J. Fernández-Rossier, *2D Materials* **4**, 035002 (2017).
- [55] T. A. Tartaglia, J. N. Tang, J. L. Lado, F. Bahrami, M. Abramchuk, G. T. McCandless, M. C. Doyle, K. S. Burch, Y. Ran, J. L. Y. Chan, and F. Tafti, *Sci. Adv.* **6**, eabb9379 (2020).
- [56] P. Jadaun, L. F. Register, and S. K. Banerjee, *npj Comput. Mater.* **6**, 88 (2020).
- [57] W. Du, K. Dou, Z. He, Y. Dai, B. Huang, and Y. Ma, *Nano Lett.* **22**, 3440 (2022).